Journal of Materials Chemistry A

Accepted Manuscript

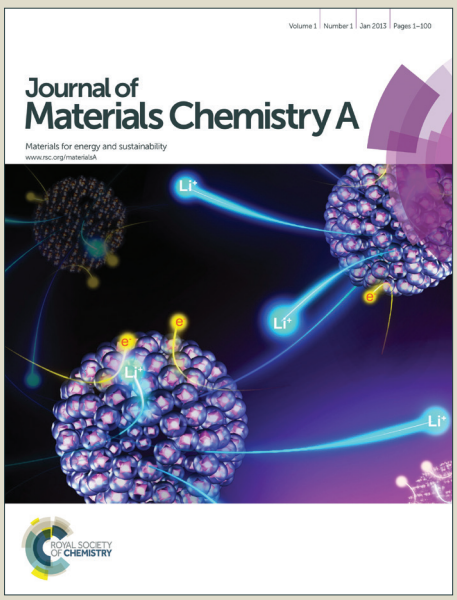

ROYAL SOCIETY OF CHEMISTRY

www.rsc.org/materialsA

Journal of Materials Chemistry A

ARTICLE

Surface Functionalized Manganese Ferrite Nanocrystals for Enhanced Uranium Sorption and Separation in Water

Received 00th January 20xx,
Accepted 00th January 20xx

DOI: 10.1039/x0xx00000x

www.rsc.org/

Seung Soo Lee,[a] Wenlu Li,[a] Changwoo Kim,[a] Minjung Cho,[b] Brandon J. Lafferty,[c] and John D. Fortner[a,*]

Developments in nanoscale engineering now allow for molecular scale optimization of reactivity, sorption, and magnetism, among other properties, for advanced, material-based environmental applications, including sorption, separation, and sensing of radionuclides. Herein, we describe novel, monodisperse nanoscale manganese ferrite crystals ($MnFe_2O_4$) for ultra-high capacity environmental sorption and subsequent separation of uranyl in water. System optimization was explored as a function of nanocrystal (core) composition, surface coating(s), and water chemistry. 11 nm $MnFe_2O_4$ nanocrystals, which were colloidally stabilized via engineered oleyl-based surface bilayers, demonstrate extreme, yet specific, uranium binding capacities while remaining monomerically stable under environmentally relevant conditions (water chemistries), which are key for application. In particular, $MnFe_2O_4$ cores with oleyl phosphate (as the outer facing layer) bilayers demonstrate preferential uranium binding of > 150% (uranium weight) / (particle system weight) while being highly water stable in elevated ionic strengths/types and pH (up to 235.4 ppm (10.24 mM) of NaCl and 51.3 ppm (1.28 mM) of $CaCl_2$, in addition to 60 ppm of Uranyl, pH 5-9). Further, when normalized for size and surface coatings, $MnFe_2O_4$ nanocrystals had significantly enhanced sorption capacities compared to Mn_2FeO_4, Fe_3O_4 and manganese oxide core analogs. Mechanistically, we demonstrate that observed uranium sorption enhancement is due to not only to thermodynamically favorable interfacial interactions (for both particle and selected bilayer coatings), but also due to significant uranyl reduction at the particle interface itself. Uranium sorption capacities for optimized systems described are the highest of any material reported to date.

1. Introduction

Magnetic metal oxide nanocrystals, including iron- and manganese oxides, have shown considerable potential for application in radionuclide sorption, separation, sensing, and stabilization, all of which remain critical challenges for a number of disciplines.[1-8] For uranium in particular, such nanoscale oxide materials have demonstrated high sorption capacities due to both high surface to volume ratios, thermodynamically favorable surface chemistries (for chemisorption), and enhanced (surface) redox potentials. Varied oxidation states of surface transition metal ions (iron (II and II) and manganese (II, III, and IV) underpin such processes including facile reduction and thus immobilization of soluble uranyl (VI) as uranium (IV) precipitates.[9-15] Interestingly, specifically designed binary and ternary oxide analogs, with engineered surfaces, such as manganese-iron mixed (ferrite) metal oxide materials, have not been similarly evaluated, despite typically being more reactive than mono-oxide analogs.[16, 17] Further, engineering surface coatings for improved material stability (in water) while concurrently enhancing uranium sorption provides additional optimization space.

Manganese ferrites are a cubic spinel crystal structure consisting of face closed packed oxygen with manganese and iron ions having oxidation states of 2+ and 3+ in either tetrahedral or octahedral sites.[18-20] Alloyed manganese iron oxide structures with $Mn^{2+}Fe_2^{3+}O_4^{2-}$ composition form by the replacement of Fe^{2+} with Mn^{2+} within the crystal lattice at varied ratios. Ferrite nanocrystals can be prepared using ionic metal precursors as metal chlorides or nitrates which are hydrated *via* reverse micelles, hydrothermal, or coprecipitation methods based on efficacy and cost.[21-28] Among these processes, thermal decomposition routes, by which temperature and precursor ratios can be highly controlled, allow for systematic development of uniform manganese, cobalt and nickel ferrite nanocrystals with narrow diameter distributions (σ < 10%) and particle size control.[29-33]

[a] Department of Energy, Environmental, and Chemical Engineering, Washington University, St. Louis, MO63130, USA. E-mail: jfortner@wustl.edu
[b] Department of Translational Imaging and Department of Nanomedicine, Houston Methodist Research Institute, Houston, TX77030, USA
[c] Engineer Research and Development Center, US. Army Corps of Engineers, Vicksburg, MS39180, USA
† Electronic Supplementary Information (ESI) available: See
DOI: 10.1039/x0xx00000x

Herein, we explore uranium sorption behavior for serially developed engineered monodisperse manganese ferrite nanocrystals ($MnFe_2O_4$), which are water stabilized *via* ordered organic surface coatings. Decomposition of metal oleate precursors (both manganese and iron oleates) at 320 ^{o}C resulted in monodisperse manganese ferrite nanocrystals with varying composition ratios of manganese to iron (from iron rich manganese ferrite ($Mn_{0.2}Fe_{2.8}O_4$) to manganese rich manganese ferrite ($Mn_{2.9}Fe_{0.1}O_4$)). Synthesized nanocrystals were phase transferred to water through ligand (ordered bilayers) encapsulation and ligand (single layer) exchange methods for aqueous-based uranium sorption evaluation(s) under environmentally relevant aqueous chemistries (pH and ionic strength/type). Materials surface stabilized with oleyl (based) molecules demonstrated significant, yet specific, uranium sorption capacities in addition to high colloidal stabilities in model waters. Mechanistically, we show that, in addition to ligand and surface (ligand) binding, uranyl (VI) is observed to undergo significant reduction to U(IV) at the ferrite interface. Uranyl sorption capacities observed for these materials are the highest of any material reported to date.[34-37]

2. Experimental

2.1 Chemicals

Iron (III) chloride hexahydrate ($FeCl_3 \bullet 6H_2O$, 97%), Manganese (II) chloride tetrahydrate ($MnCl_2 \bullet 4H_2O$, 99.99 %), oleic acid (OA, 90 %), 1-octadecene (90 %), poly (ethyleneglycol) (PEG, Mw = 200), octadecylphosphonic acid (ODP, 97 %), stearic acid (SA, 98.5 %), octadecylsulfate (ODS, 93 %), CTAB, manganese (II) oxide (MnO, 99 %), iron (II, III) oxide (Fe_3O_4, 97%), manganese iron oxide ($MnFe_2O_4$, 99 %) were purchased from Sigma-Aldrich. Oleylphosphate (OP) was purchased and sodium oleate (97 %) was purchased from TCI America. Uranyl nitrate hexahydrate ($UO_2(NO_3)_2 \bullet 6H_2O$) was purchased from Antec, Inc. All nanocrystals were synthesized under nitrogen condition (N_2, 99.999%).

2.2 Synthesis of Nanocrystalline Iron Oxides, Manganese Oxides, and Manganese Iron Oxides (Ferrites)

11 nm magnetic metal oxides were synthesized by metal precursor decomposition at high temperature by the method reported previously.[33] For iron oxide nanocrystals, 2 mmol of FeOOH were used as an iron precursor and decomposed in the presence of 8 mmol of oleic acid in 8 g of 1-octadecene at 320 ^{o}C for 1h.[38] Manganese oxide nanocrystals were synthesized by decomposition of 3.0 mmol of manganese oleate with 1.5 mmol of oleic acid in 5 g of 1-octadecene at 320 ^{o}C for 1h.[14] Manganese iron oxide nanocrystals were synthesized by decomposition of the mixture of metal oleate precursors (0.27 mmol of manganese oleate and 0.72 mmol of iron oleate as metal precursors) with excess oleic acid (2 mmol) in 5 g of 1-octadecene at 320 ^{o}C for 1 h; the composition of the nanocrystal between iron and manganese were controlled by the ratio between two different metal precursors. The resulting nanocrystals were purified using ethanol, acetone, and hexane; nearly 0.5 g of the resulting colloidal nanocrystals was mixed with 5 ml of hexane, 10 ml of ethanol, and 30 ml of acetone and centrifuged at 8000 rpm for 20 min. This process was repeated three times. The purified black colloids were well dispersed in various nonpolar solvents such as, chloroform, hexane, and toluene.

2.3 Phase Transfer of Engineered Nanocrystals: Single Layered Nanocrystals

The as-synthesized nanocrystal was phase transferred to aqueous phase *via* single and bilayer methods (ligand exchange and ligand encapsulation).[39-41] For the formation of the single layered nanocrystal structure, the as synthesized nanocrystals were coated with poly (ethylene glycol) with 200 molecular weights (PEG200) by ligand exchange method. More specifically, a particular amount of PEG200 (30.0 mg of PEG200) was mixed with 0.5 ml nanocrystal solution (1.5×10^{18} nanocrystals/L) in hexane and 6 ml of ultra-pure water (MILLIPORE, 18.2 MΩcm). Aqueous and organic phases were mixed and sonicated using a probe-sonicator (UP 50H, Hielscher) for 5 min at 80 % amplitude, full cycle. The resulting nano colloid suspensions were further stirred for 1 day under vacuum condition to evaporate hexane and to obtain a clear brownish black solution. The phase transferred nanocrystal suspensions were, then, separated from excess (free) organic phase transfer agent molecules using ultracentrifugation (Sorvall WX Ultra 80, Thermo scientific) at 60,000 rpm for 2 h, and membrane filtration (Ultrafiltration cellulose membranes, 100 KDa MWCO) using a stirred cell (Amicon), followed by syringe filtration (0.22 μm, PTFE, Whatman). The transfer yield of the final solution was over 60 %.

2.4 Phase Transfer of Engineered Nanocrystals: Bilayered Nanocrystals

0.05 mmol of surface stabilizers (oleyl phosphate, oleic acid, octadecylphosphonic acid, stearic acid, SDS, and CTAB) were added to 0.5 ml of nanocrystal in hexane solution (particular nanocrystal concentration was 1.5×10^{18} nanocrystals/L) and mixed with 6 ml of ultra-pure water (Millipore, 18.2 MΩcm). The aqueous and organic mixture was, then, probe sonicated and purified by ultracentrifugation, membrane filtration, and syringe filtration as mentioned above. In all cases, the transfer yield of each of the purified nanocrystal was over 70 %.

2.5 Dynamic Light Scattering

The hydrodynamic diameters and surface charge of the phase transferred engineered nanocrystals (iron oxides, manganese oxides, and manganese iron oxides) with single- and bi-layered surface coating structures were measured at pH 7.2 and 25 ^{o}C, using a Malvern Nano ZS system by Malvern Instruments equipped with a HeNe 633 nm laser (Malvern Zetasizer Nanoseries, Malvern, UK). The average hydrodynamic diameters were obtained by the mean size of the first peak of the number distribution and the standard deviation was determined from triplicate measurements.

2.6 Transmission Electron Microscope (TEM)

The diameters of the as-synthesized nanocrystals were measured through transmission electron microscope (TEM). TEM specimens were prepared using carbon support film on 300 mesh copper grids (electron Microscopy Sciences). The TEM micrographs were taken by a Tecnai G2 Spirit Twin microscope (FEI, Hillsboro, OR) operated at 120 kV. HRTEM analysis was performed using a JEOL 2100F microscope (JEOL. Tokyo, Japan) operated at 200 kV. The size and size distribution data were obtained by counting over 1000 nanocrystals using Image-Pro Plus 5.0.[42]

2.7 X-Ray Diffraction (XRD)

X-ray powder diffraction (XRD) patterns were obtained using a Rigaku D/Max/A. 2θ range was from 10 to 80 degree with a Cu Kα radiation (1.54 Å) and the X-ray was generated at 40 kV and 40 mA.

2.8 Inductively Coupled Plasma -Optical Emission/-Mass Spectroscopy (ICP-OES/-MS)

The particle concentrations were measured by an inductively coupled plasma optical emission spectrometer (CP-OES, Perkin Elmer Optima 7300DV) equipped with an autosampler. Bound and soluble uranium was measured by an inductively coupled plasma mass spectrometer (ICP-MS, Perkin Elmer ELAN DRC II) also equipped with autosampler. For both, samples were first acidified with 1% nitric acid before analyses.

2.9 Uranium Sorption Measurement

To evaluate uranium adsorption properties of phase transferred manganese ferrite nanocrystals, the nanocrystal samples (typically nanocrystal concentration was 2.3×10^{15} nanocrystals/L) were mixed with uranium (from 0.1 to 40 ppm) at three different pH conditions (5.6, 7.0, and 8.5) and equilibrated on a rotating rack that tumbled end-over-end for 24h. The nanocrystals were, then, separated using ultracentrifugation at 40,000 rpm for 2 h and the remaining concentrations of uranium (VI) in the supernatant solution were analysed by ICP-MS. These measurements were conducted in triplicates. The measured uranium sorption capacity values (mass of adsorbed uranium per mass of nanocrystals in the sample) as a function of equilibrium concentration of uranium (mg/L) were best fitted with the plot drawn by the Langmuir isotherm equation:

$$q_e = \frac{q_{max} k \mathrm{C}_e}{(1 + k\mathrm{C}_e)}$$

where q_e is the amount of adsorbed uranium at equilibrium concentration (mg/g), k is the sorption constant, q_{max} is the maximum sorption density (mg/g; mass of the sorbed uranium per mass of manganese), and C_e is the equilibrium concentration of uranium.

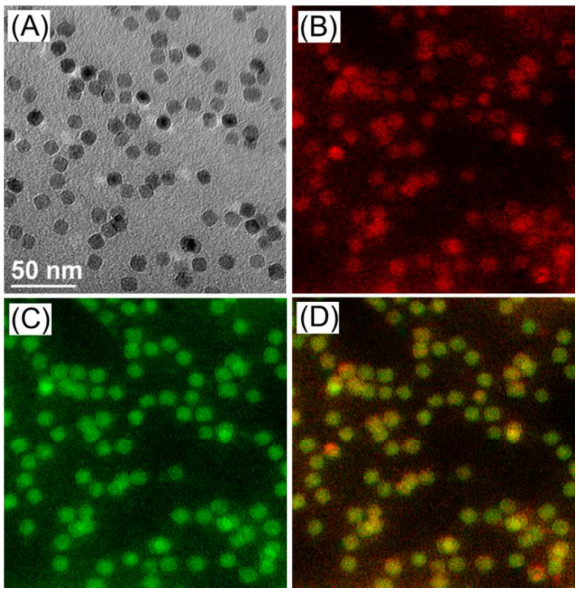

Fig 1. Monodisperse $MnFe_2O_4$ nanocrsytal. The diameter of the nanocrystalline $MnFe_2O_4$ is 11.0 ± 1.0 nm measured by counting over 1000 nanoparticles using Image-Pro plus 6 (A). Gatan Image Filter (GIF) analysis shows the mapping position of two different metals, iron (B, Red) and manganese (C, green), is identical in the same spherical (D, mixed with red and green).

2.10 Critical Coagulation Concentration (CCC)

Nanocrystal aggregation kinetics were examined by monitoring hydrodynamic diameters of phase transferred manganese ferrite nanocrystals (typically, 2.5×10^{12} nanocrystals per milliliter) in varied concentration of NaCl (from 50 to 1000 mM) and $CaCl_2$ (from 1 to 40 mM) at pH 7.0 for 40 min. The attachment efficiency of the nanocrystal aggregates, α, in the presence of monovalent or divalent salt suspension was calculated by the equation below:

$$\alpha = \frac{k}{k_{\mathrm{fast}}}$$

where k is the initial aggregation rate constant at elevating salt concentrations and k_{fast} is the diffusion limited aggregation rate constant under favorable aggregation conditions. [43-47]

3. Results and Discussion

3.1 Synthesis and Phase Transfer of Manganese Ferrite Nanocrystals

Manganese iron oxides (manganese ferrites) were precisely synthesized via incorporation of divalent manganese, Mn^{2+}, into the spinel lattice structure of an iron oxide via thermal decomposition of manganese and iron precursors at a temperature over 300 °C. This procedure is similar to the synthetic method of various binary ferrite nanocrystals

($M_xFe_yO_4$, M = Mg, Cr, Fe, Co, Ni, and Zn) through non-aqueous, high temperature processes.[27, 29-31, 48-53] For materials described, we used mixed metal precursors of iron and manganese oleates in the presence of oleic acid, which acts as a surface stabilizer (in 1-octadecene). Both manganese and iron oleates, begin decomposing at elevated temperature (240~260 °C) with monodispersed nanocrystals (under 10 % dispersity) forming at 320 °C, while allowing for controllable molar ratios between (final) manganese and iron particle content(s). As shown in Fig 1, as synthesized $MnFe_2O_4$ nanocrystals (11.0 ± 1.0 nm) are Mn-Fe alloyed crystal structures (with iron (red) and manganese (green)). The composition between manganese and iron of the nanocrystal was be systematically controlled by the ratio of manganese oleate to iron oleate during synthesis; increasing ratio of manganese to iron precursors resulted in the higher ratio of manganese to iron in the final nanocrystals (Fig S1, ESI†). High resolution-transmission electron microscopy (HR-TEM) images of manganese ferrite nanocrystals indicated a high degree of crystallinity with a lattice distance (311) plane of 0.252 nm (Fig S3, ESI†). XRD diffraction analysis indicated that iron rich manganese ferrite ($MnFe_2O_4$) and manganese rich ferrite (Mn_2FeO_4) nanocrystals are similar in structure to parent Fe_3O_4 and manganese oxide (Mn_xO_y as $MnO@Mn_3O_4$) but shifted, as expected, when mixed (Fig S2, ESI†).[14, 31]

For aqueous applications, synthesized materials must be phase transferred from the organic reaction matrix into water. To do this, ligand encapsulation and exchange methods were used to render the surface of the nanocrystals effectively hydrophilic.[39, 41] By capping nanocrystals with oleic acid (hydrophobic tail facing outwards) in nonpolar organic solvents (1-octadecene and/or hexane), as-synthesized nanocrystal can be subsequently surface tailored with a second organic layer (forming a bilayer complex). The second, outward facing molecular layer, which is typically a long chain (C8-C20) organic acid (head group), is stabilized through van der Waals forces with the hydrophobic tail of the oleic acid, with outward facing, hydrophilic head (functional) groups (phosphate, carboxyl, sulfonyl, amine group, etc.) as depicted in Fig 2. Additionally, the hydrophobic surface coatings (oleic acids) on as-synthesized nanocrystal can simply be replaced at the surface with hydrophilic surface coating materials, such as poly (ethylene glycol), via ligand exchange methods.[40] Based on such strategies, not only can engineered nanocrystal surfaces be systematically 'flipped' from hydrophobic to hydrophilic, but also allow for controlled surface coating thickness, functionality (head) group, and net surface charge. Such flexibility is demonstrated here using oleyl phosphate (OP), octadecyl phosphonic acid (ODP), oleic acid (OA), stearic acid (SA), octadecyl sulphate (ODS), cetyltrimethylammonium bromide (CTAB), and polyethylene glycol (PEG) with a molecular weight of 200 (PEG200).

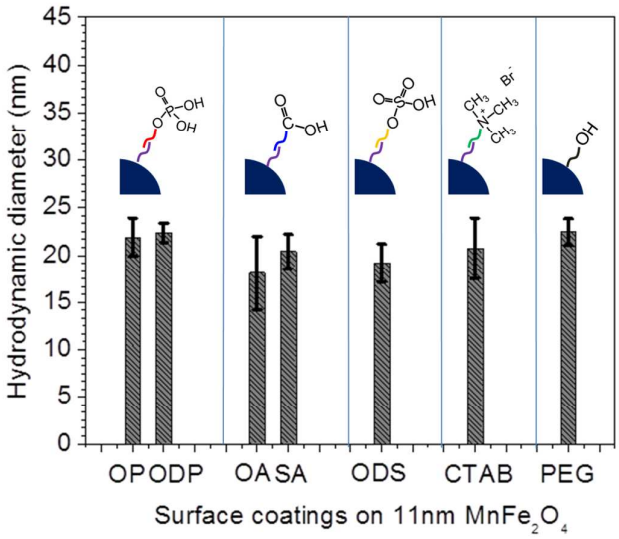

Fig 2. Hydrodynamic diameters of phase transferred manganese iron oxide ($MnFe_2O_4$) nanocrystals. 12 nm nanocrystals measured by TEM images were coated with various surface stabilizers; bilayered surface coating structures were achieved by surface encapsulation method using phosphonic acid functionalized (oleyl phosphate (OP) and octadecylphosphonic acid (ODP)), carboxylic acid functionalized (oleic acid (OA) and stearic acid (SA)), sulfate functionalized (octadecyl sulfate (ODS)), and amine group functionalized (CTAB) surface stabilizers. Single layered surface coating structures were formed by ligand exchange method using polyethylene glycol (PEG200). The average hydrodynamic diameters of all phase transferred nanocrystal samples were from 18 to 22 nm.

Fig 2 depicts the structure and surface functionality of prepared material libraries with single and double (bi-) layered surface coatings. Resulting water-stable particles were characterized by dynamic light scattering (DLS) and zeta potential measurements to determine the hydrodynamic size and surface charge, respectively. DLS measurements indicate thin and compact surface structures for all coatings evaluated (organic acid containing 18 carbon chains (both saturated and unsaturated carbon chains) and low molecular weight polyethylene glycol (PEG 200)). Oleyl phosphate, octadecylphosphonic acid, oleic acid, stearic acid, octadecyl sulfate, CTAB, and PEG200 coated nanocrystalline manganese ferrites of 11nm core diameter showed hydrodynamic diameters of 21.9 ± 2.0, 22.4 ± 1.0, 18.1 ± 3.9, 20.4 ± 1.8, 19.2 ± 2.0, 20.7 ± 3.2, and 22.5 ± 1.4 nm, respectively. The zeta potential of oleyl phosphate, octadecylphosphonic acid, oleic acid, stearic acid, octadecyl sulfate, CTAB, and PEG200 coated manganese oxide nanocrystals were -62.9 ± 1.7, -43.0 ± 1.9, -46.7 ± 0.7, -37.9 ± 4.7, -48.5 ± 3.3, 54.8 ± 1.5, and -14.7 ±1.6 mV, respectively.

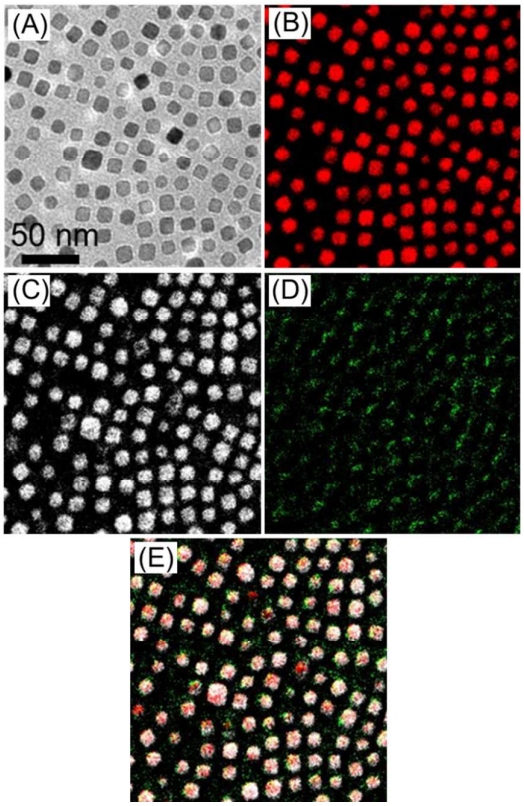

Fig 3. Elemental mapping in uranium adsorbed manganese iron oxide nanocrystals ($MnFe_2O_4$@OP). The nanocrystal samples after uranium sorption measurements were analyzed by TEM (A) and each element (iron (red, B), manganese (white, C), uranium (green, D), and mixed with every element (E)) were analyzed by Gatan Image Filter (GIF) analysis.

Colloidal stability, which is key for aqueous applicability, of stabilized nanocrystalline manganese ferrites was examined in terms of nanocrystal aggregation kinetics in the presence of environmentally relevant salts. As shown in Fig S4 (ESI†), the hydrodynamic diameter of the nanocrystals were monitored as a function of time in the presence of increasing ionic strengths (using sodium and calcium) to determine the critical coagulation concentrations (CCC) for each nanocrystal sample.[43, 44, 46, 47] Relatively high CCC values (i.e. high particle stability) were observed for ferrite nanocrystals coated with unsaturated–unsaturated (C18 carbon surfactants with a C9-C10 *cis* double bond, typical for a number of oleyl-based molecules) carbon chain linked bilayered surface coating structures, such as oleic acid bilayered $MnFe_2O_4$ ($MnFe_2O_4$@OA) and oleic acid–oleylphosphate linked $MnFe_2O_4$ ($MnFe_2O_4$@OP), as shown in Fig S4 (ESI†). In comparison, particles with unsaturated– saturated bilayer structures (unsaturated oleic acid and an outward facing, saturated (sp3) C18 linear carbon chain with varied head groups (e.g. $MnFe_2O_4$@SA, $MnFe_2O_4$@ODP, and $MnFe_2O_4$@ODS)) and pegylated surfaces were observed to have relatively lower particle stabilities, via CCC evaluation. We hypothesize that the *cis* (oleyl) forms of unsaturated – unsaturated oleyl carbon chains enhances bilayer structure stability due, in part, to increased order and van der Waals interactions, and thus lower (molecular) degree(s) of freedom for the second layer, compared to unsaturated–saturated carbon chains.[39] Prakash et al. also reported high colloidal stability of similar unsaturated – unsaturated carbon chain linked bilayered surfaces (compact oleic acid bilayer surface coatings) for nanocrystalline oxide materials at varied pH (from 4 to 10), ionic strength (from 0.01 to 1 M), and temperature (from 10 to 100 ^{o}C).[39] As shown in Fig S4 (ESI†), CCC values of NaCl and $CaCl_2$ for each nanocrystal structure were 665.8 mM of NaCl and 16.4 mM of $CaCl_2$ for $MnFe_2O_4$@OA, 617.4mM of NaCl and 15.9 mM of $CaCl_2$ for $MnFe_2O_4$@OP, 301.8 mM of NaCl and 7.8 mM of $CaCl_2$ for $MnFe_2O_4$@SA, 297.9 mM of NaCl and 7.7 mM of $CaCl_2$ for $MnFe_2O_4$@ODP, 367.0 mM of NaCl and 8.3 mM of $CaCl_2$ for $MnFe_2O_4$@ODS, and 239.0 mM of NaCl and 6.8 mM of $CaCl_2$ for $MnFe_2O_4$@PEG.

3.2 Uranium Sorption

Water stabilized monodisperse manganese ferrite nanocrystals were evaluated for uranium adsorption and separation performance under environmentally relevant, aqueous conditions (at varied pH and ionic strength conditions). As shown in Fig 3, uranium adsorption (by 11 nm $MnFe_2O_4$@OP) was qualitatively observed by elemental mapping analysis (GIF analysis), visualizing each element (manganese, iron, and uranium) after separation at the end of a sorption experiment (24 h batch sorption experiment). To systematically quantify sorption, batch isotherm experiments, exploring the roles of surface coating and the ferrite composition under environmentally relevant aquatic conditions, were compared. It is hypothesized that uranyl can be sorbed by both the surface coating (e.g. a functional group) via electrostatic interaction and also bound to the surface inorganic core by coordinated physical-chemical sorption, which can be enhanced through redox reactions (Fig 4).[2, 9, 12, 13, 54, 55]

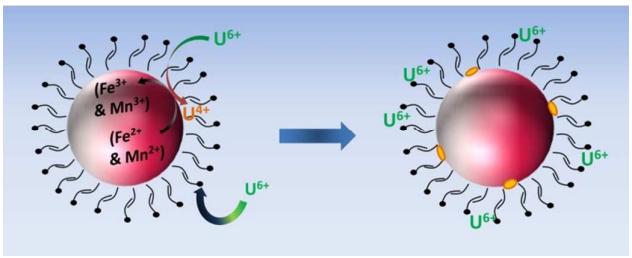

Fig 4. Uranium adsorption on the nanocrystalline $MnFe_2O_4$. Uranium species with high oxidation state (uranyl; U(VI), green) may bind to the negatively charged surface functional group of the nanocrystal by electrostatic interaction. When uranium (VI) meets with divalent metal ions (Fe (II) and/or Mn (II)) on the surface of the inorganic core of the nanocrystal structure, uranium (VI) is reduced, forming un-soluble precipitate (U(IV), orange).

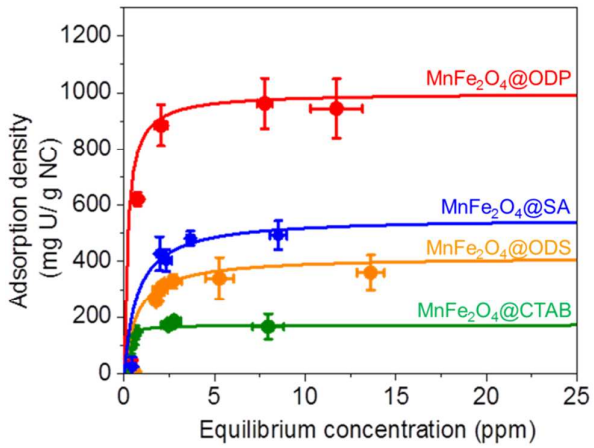

Fig 5. Uranium sorption isotherm on bilayer structured (unsaturated–saturated carbon chain linked) $MnFe_2O_4$ nanocrystals. Uranium sorption measurements were performed on the nanocrystal samples coated with octadecylphosphonic acid (ODP, red), stearic acid (SA, blue), octadecylsulfate (ODS, yellow), and CTAB (green); typical nanocrystal concentration was 2.3×10^{15} nanocrystals/L in each sample) at uranium (U(VI)) concentration from 0.1 to 40 mg/L at pH 7.0. All calculated uranium sorption capacity values were fitted by Langmuir isotherm equation (solid lines).

For functional group and charge dependent uranium adsorption measurements, the $MnFe_2O_4$ core was coated with varied bilayered surface structures (as phosphonic acid, carboxylic acid, sulfate and amine group functionalized) and evaluated at pH 5-9 (pH 7 results are shown in Fig 5). The highest uranium sorption capacity of ca. 1000 mg U/g NC (milligram of U per gram of nanocrystals) was found to occur with a phosphonic acid group functionalized manganese ferrites ($MnFe_2O_4$@ODP); other negatively charged nanocrystal samples such as, stearic acid (SA) and octadecylsulphate (ODS) coated nanocrystals showed 555.6, and 400.0 mg U/g NC, respectively (Table S2). The lowest adsorption value of uranium (172.4 mg U/g NC) was observed from the positively charged manganese ferrite nanocrystals ($MnFe_2O_4$@CTAB). Strong binding affinities of uranyl (UO_2^{2+} and $UO_2(OH)^+$) to phosphonic acid and carboxyl groups is expected based on both electrostatic potentials and favorable uranyl-phosphate complexation chemistries.[56-59]

Interestingly, when the phase (surface) transfer agents (phosphonic acid or carboxyl group containing organic acid) is in the form of an unsaturated carbon (oleyl-like) chains $MnFe_2O_4$ nanocrystal revealed even higher uranium sorption capacities, compared to the saturated analogs: 1250 mg U/g NC for oleyl phosphate coated- and 666.7 mg U/g NC of oleic acid coated- bilayer structured $MnFe_2O_4$ nanocrystals at pH 7 and upwards of 1667 mg U/g NC at pH 5 ($MnFe_2O_4$, with oleyl phosphate outer layer) as shown in Fig 6A and Table S3. Such an increase in sorption is hypothesized to occur, in part, due to the enhanced particle stabilities for oleyl-based bilayer structures, as discussed above.

As shown in Fig 6B, the hydrodynamic diameters of both the saturated-unsaturated and the unsaturated–unsaturated carbon chains linked bilayered $MnFe_2O_4$ nanocrystals were monitored as a function of uranium concentrations ranging from 0.1 to 40 ppm (from 4.25×10^{-4} to 0.17 mM after 24 h batch experiments. Both oleylphosphate-oleic acid and oleic acid-oleic acid linked bilayered $MnFe_2O_4$ nanocrystals maintained their colloidal stability over all concentrations evaluated.

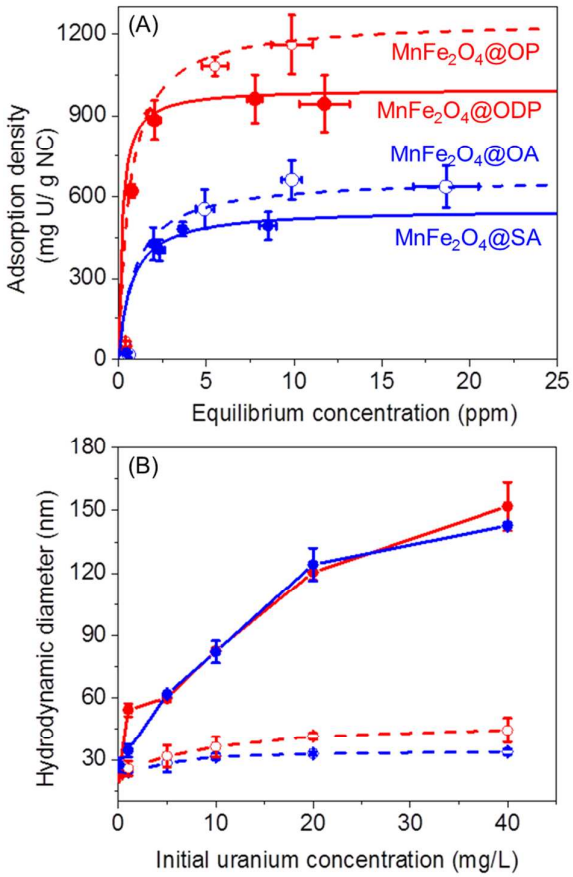

Fig 6. Comparison of uranium adsorption on bilayer structured (unsaturated– saturated (red and blue solid lines) vs. unsaturated–unsaturated (red and blue dotted lines) carbon chain linked) $MnFe_2O_4$ nanocrystals. (A) Uranium sorption measurements were performed with nanocrystal samples coated with oleyl phosphate (OP, red dot line), octadecylphosphonic acid (ODP, red solid line), oleic acid (OA, blue dot line), and stearic acid (SA, blue solid line); typical nanocrystal concentration was 2.3×10^{15} nanocrystals/L with uranium (U(VI)) concentration from 0.1 to 40 mg/L at pH 7.0. All calculated uranium sorption capacity values were fitted by Langmuir isotherm equation. (B) Hydrodynamic diameters of each sample was monitored at elevated uranium concentration from 0.1 to 40 ppm of U(VI).

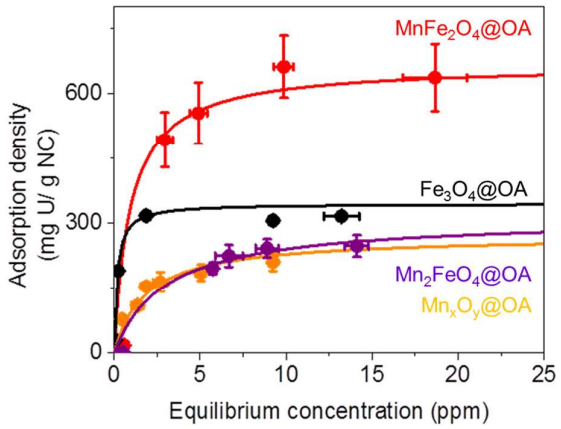

Fig 7. Uranium sorption isotherm on composition controlled manganese iron oxide nanocrystals. Uranium sorption measurements were performed on oleic acid (OA) bilayered nanocrystals samples ($MnFe_2O_4$ (red), Fe_3O_4 (black), Mn_2FeO_4 (purple), and Mn_xO_y (yellow)); typical nanocrystal concentration was 2.3×10^{15} nanocrystals/L in each sample) at uranium (U(VI)) concentration from 0.1 to 40 mg/L at pH 7.0. All calculated uranium sorption capacity values were fitted by Langmuir isotherm equation.

Conversely, the saturated-unsaturated (ODP, SA) carbon chains linked bilayered nanocrystals readily aggregated in the presence of positively charged uranyl with resulting hydrodynamic diameters over 150 nm. These results are consistent with the critical coagulation concentration values in the presence of mono-/di-valent (Na^+/Ca^{2+}) cations for libraries of the phase transferred nanocrystalline $MnFe_2O_4$. The highest (i.e. most stable) critical coagulation concentration values (over 600 mM of Na^+ and 16 mM of Ca^{2+}) were observed with unsaturated carbon chain linked bilayered $MnFe_2O_4$ nanocrystals (both oleyl phosphate coated- and oleic acid coated- bilayered nanocrystals) (Fig S4, ESI†).

Uranium sorption capacities of manganese ferrites were also evaluated as a function of the ferrite composition (i.e. ratio of manganese and iron) for 11 nm particles which were all stabilized by an oleic acid bilayer at pH 7. $MnFe_2O_4$ cores demonstrated the highest capacity (666.7 mg U / g NC for $MnFe_2O_4$) compared with Mn_2FeO_4, Mn_xO_y, and Fe_3O_4 (312.5, 270.3, and 344.8 mg U / g NC, respectively) (Fig 7, Table S4). Enhanced uranium sorption capacity of $MnFe_2O_4$ is in part due to the enhanced reduction from uranium (VI) to uranium (IV) at the interface between the nanocrystal and uranium ion via partial redox reactions.

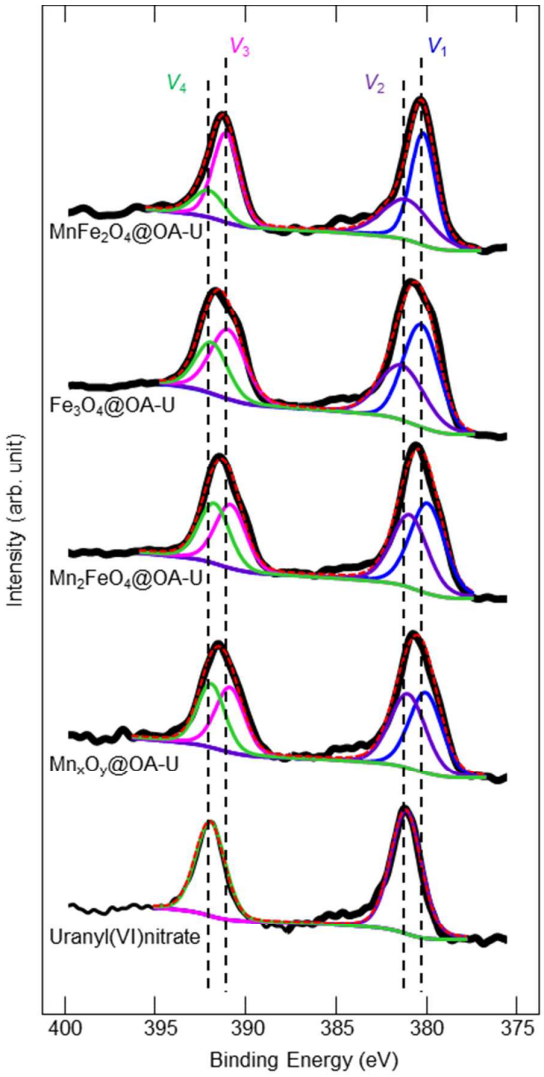

Fig 8. Redox reaction of uranium (U) on the surface of the composition controlled nanocrystals. The black lines are the raw data and the red dash lines are the fitted curves based on curve fitting using V_1 (blue), V_2 (purple), V_3(pink), and V_4(green). The ratio of U(IV) to U(VI) was calculated by $(V_1+V_3)/(V_2+V_4)$ in the uranium 4f XPS data from the sample after the uranium sorption measurement and compared with uranium nitrate (Table S5).

The uranium 4f XPS data of the materials sampled before and after uranium sorption measurements show the highest uranium reduction (total) for $MnFe_2O_4$ (iron rich ferrite) cores with 65 % of measured U as reduced uranium (IV) (from uranium (VI)) (Fig 8); the uranium reduction percentage of Fe_3O_4, Mn_2FeO_4, and Mn_xO_y was 58 %, 53 %, and 51 %, respectively (Table S5). Accordingly, we hypothesize that for mixed ferrite nanocrystal systems, concentrations of both manganese (II) and iron (II) on the surface of the nanocrystal samples may have significant role in uranium reduction from

VI to IV (Fig 7). XPS data of manganese 2P and iron 2P shows that 17 % of Manganese (II) and 38% of iron (II) on the surface of $MnFe_2O_4$ were correspondingly oxidized upon U sorption (Tables S6, S7, and Fig S5) further supporting a surface redox mediated process. Comparatively, Mn_2FeO_4 showed less (relative) change in oxidation of both manganese (II) and iron (II) (2 % of Fe (II) and 4% of Mn (II) were oxidized) due to lower concentration of manganese (II) and iron (II) on the surface of the pristine manganese rich ferrite nanocrystal (Tables S6, S7, and Fig S5). For pure iron oxide and manganese oxides, 43 % of iron (II) for iron oxide and 6 % of manganese (II) for manganese oxide samples were oxidized after uranium adsorption measurements (Tables S6, S7, and Fig S5). Finally, for comparison, commercial metal oxide nanocrystal (no surface coatings) analogs were observed to sorb 6.6 mg U / g NC for manganese ferrite, 4.9 mg U / g NC for iron oxide (magnetite) and 4.4 mg U / g NC for manganese oxide (MnO) at pH 7. In water, uncoated, commercial magnetite nanocrystal samples exhibited significant and rapid aggregation, as shown in TEM inset images in Fig S6 (ESI†), thus lower surface area for sorption / reaction processes to occur.

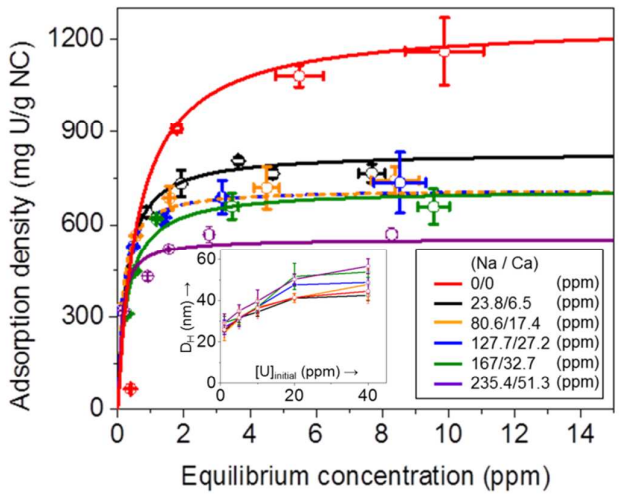

Fig 9. Uranium sorption isotherm on $MnFe_2O_4$@OP nanocrystals at elevated ionic salt concentrations. Uranium sorption measurements were performed on the nanocrystal samples in the presence of both sodium and calcium with the ratio of 5 to 1; typical nanocrystal concentration was 2.3×10^{15} nanocrystals/L in each sample at uranium (U(VI)) concentration from 0.1 to 40 mg/L at pH 7.0. The inset image shows the hydrodynamic diameters (D_H) of the nanocrystals as a function of initial uranium concentration ($[U]_{initial}$) at elevated both sodium and calcium concentrations. All calculated uranium sorption capacity values were fitted by Langmuir isotherm equation.

3.3 Effects of Ionic Strength and pH

To understand how water chemistry affects uranium adsorption properties, we investigated uranium adsorption as a function of ionic strength and type (both sodium and calcium) and pH. Fig 9 shows uranium sorption capacities of oleyl phosphate coated bilayered $MnFe_2O_4$ nanocrystals in the presence of sodium (from 0 to 235 ppm (10.2 mM)) and calcium (from 0 to 51 ppm (1.28 mM)) with a mole ratio of ca. 10/1 between sodium and calcium. In general, U adsorption capacity of the phosphate group functionalized nanocrystalline $MnFe_2O_4$ decreased as ionic salt (both sodium and calcium) concentrations increased; with a ca. 55% decrease in sorption capacity at high salt concentrations (235.4 ppm (10.24 mM) of sodium with 51.3 ppm (1.28 mM) of calcium) (Table S8). For reference a typical ground water has ca. 125 ppm (5.44 mM) of sodium and ca. 24 ppm (0.60 mM) of calcium.[60] The decrease in uranium sorption capacities for multi-cationic mixtures may not only arise from nanocrystal aggregation as shown for the DLS measurements in Fig 9 (inset) but also due to binding site competition.[34, 60]

To evaluate the multi-sorbate (competitive) effects for oleyl phosphate coated $MnFe_2O_4$ nanocrystals, we explored sodium and calcium particle sorption (by measuring remaining sodium and calcium concentrations) at varied uranyl concentrations, upon equilibrium and separation. As shown in Fig S7 (ESI†), the highest sorption values for both calcium and sodium were observed when the initial (competitive) uranium concentration was low (< 5 ppm); sorbed sodium and calcium concentrations on the nanocrystals were observed to reach up to 125 ppm (system) of sodium (14.8 g Na / g NC) and 42 ppm of calcium (4.9 g Ca / g NC) in the case for initial sodium and calcium concentrations of 235 and 51 ppm. Interestingly, sodium and calcium can be correspondingly released as a function of subsequent uranyl addition via displacement. For example, 60 ppm (2.61 mM) of sodium and 11 ppm (0.27 mM) of calcium ions were released from $MnFe_2O_4$@OP samples (8.44 mg/L of the nanocrystals), by 6 ppm (0.026 mM) of adsorbed uranium upon a 10 ppm (0.043 mM) uranyl injection (Fig S7 (A), ESI†).

In contract to the near complete release of surface associated sodium ions (over 90 %) released upon the introduction of excess uranyl in batch experiments, a lower percentage of calcium ions were displaced (Fig S7, ESI†). We hypothesize that relatively stronger divalent calcium cation association with negatively charged nano-sorbent systems (OP) compete with divalent cationic uranium ion (uranyl, UO_2^{2+}) binding sites. For example, there was little effect on uranium sorption capacities of $MnFe_2O_4$ coated with oleylphosphate when the nanocrystals were first exposed to excess sodium salts (only). In this case, nanocrystals remained colloidally stable and the sorption capacity was over 1000 mg U / g NC at 18,000 ppm of sodium in pH 7 water (Fig S8, ESI†). When the same nanocrystals were exposed to elevated calcium concentrations (51.3 ppm), maximum uranium adsorption capacity decreased to 714.3 mg U/ g NC at pH 7

(Fig S9 and Table S8, ESI†), which while relatively lowered, remain substantial.

4. Conclusions

Herein we describe a classic nanocrystal synthetic approach to optimize monodisperse manganese iron oxide (manganese ferrites) nanocrystals with tailorable surface chemistries for uranium sorption and separation under environmental relevant chemistries. Among the described libraries of phase (water) transferred manganese ferrite nanocrystals, oleyl phosphate (phosphonate group functionalized unsaturated carbon chain linked bilayered structure) showed the highest uranium adsorption capacities, specificity, and colloidal stability even under elevated ionic strengths and types. In core composition dependent sorption studies, $MnFe_2O_4$ nanocrystals also demonstrated significantly enhanced uranium adsorption compared to iron oxide, manganese rich manganese ferrite and manganese oxide nanocrystals (pH 7, normalized surface coatings). Mechanistically, uranium sorption was demonstrated to be due to both chemisorption and redox reactions between transition metal ions (manganese (II) and iron (II)) and uranium ions (uranium (VI) and uranium (IV)) at the particle surface. Taken together, this work highlights the platform potential for optimized/tailored, engineered particle system approach(es) for next generation actinide sorption, separation, and sensing technologies.

Acknowledgements

This work is supported by U.S. Army Corps of Engineers (W912HZ-13-2-0009-P00001), ACS Petroleum Research Fund (52640-DNI10), and the US National Science Foundation (CBET 1437820). XRD measurements were made possible by a grant from the U.S. National Science Foundation (EAR-1161543). TEM, DLS, Ultracentrifugation, ICP-OES, and ICP-MS were provided by the Nano Research Facility (NRF) at Washington University in St. Louis, a member of the National Nanotechnology Infrastructure Network (NNIN), which is supported by the National Science Foundation (ECS-0335765). The authors also thank Prof. Daniel E. Giammar for his assistance and helpful discussion.

References

1 H. Amiri, Z. Y. Zhao, T. M. Dansereau, M. A. Petrukhina, M. A. Carpenter, *J. Phys. Chem. C* 2010**, 114**, 4272-4278.
2 S. K. Biswas, A. Sarkar, A. Pathak, P. Pramanik, *Talanta* 2010**, 81**, 1607-1612.
3 S. Darshane, I. S. Mulla, *Mater. Chem. Phys.* 2010**, 119**, 319-323.
4 R. S. Hsu, W. H. Chang, J. J. Lin, *ACS Appl. Mater. Interfaces* 2010, **2**, 1349-1354.
5 L. J. Hua, J. J. Zhou, H. Y. Han, *Electrochim. Acta* 2010, **55**, 1265-1271.
6 D. R. Ingram, C. Kotsmar, K. Y. Yoon, S. Shao, C. Huh, S. L. Bryant, T. E. Milner, K. P. Johnston, *J. Colloid Interface Sci.* 2010, **351**, 225-232.
7 B. Viswanathan, P. I. Neel, T. K. Varadarajan, *Catal. Surv. Asia* 2009, **13**, 164-183.
8 Y. Zeng, T. Zhang, H. T. Fan, W. Y. Fu, G. Y. Lu, Y. M. Sui, H. B. Yang, *J. Phys. Chem. C* 2009, **113**, 19000-19004.
9 E. Liger, L. Charlet, P. Van Cappellen, *Geochim. Cosmochim. Acta* 1999, **63**, 2939-2955.
10 B. H. Jeon, B. A. Dempsey, W. D. Burgos, M. O. Barnett, E. E. Roden, *Environ. Sci.Technol.* 2005, **39**, 5642-5649.
11 T. Missana, M. Garcia-Gutierrez, V. Fernndez, *Geochim. Cosmochim. Acta* 2003, **67**, 2543-2550.
12 T. B. Scott, G. C.Allen, P. J. Heard, M. G. Randell, *Geochim. Cosmochim. Acta* 2005, **69**, 5639-5646.
13 H. Zeng, D. E. Giammar, *J. Nanopart. Res.* 2011, **13**, 3741-3754.
14 Z. Wang, S.-W. Lee, J. G. Catalano, J. S. Lezama-Pacheco, J. R. Bargar, B. M. Tebo, D. E. Giammar, *Environ. Sci. Technol.* 2012, **47**, 850-858.
15 Z. Wang, W. Xiong, B. M. Tebo, D. E. Giammar, *Environ. Sci. Technol.* 2013, **48**, 289-298.
16 J. N.Dui, G. Y. Zhu, S. M. Zhou, *ACS Appl. Mater. Interfaces* 2013, **5**, 10081-10089.
17 Y. Q. Wang, R. M. Cheng, Z. Wen, L. J. Zhao, *Eur. J. Inorg. Chem.* 2011, **19**, 2942-2947.
18 K. Raj, R. Moskowitz, *J. Magn. Magn. Mater.* 1990, **85**, 233-245.
19 A. Jordan, R. Scholz, P. Wust, H. Fahling, R. Felix, *J. Magn. Magn. Mater.* 1999, **201**, 413-419.
20 D. K. Kim, Y.Zhang, J. Kehr, T. Klason, B. Bjelke, M. Muhammed, *J. Magn. Magn. Mater.* 2001, **225**, 256-261.
21 S. Neveu, A. Bee, M. Robineau, D. Talbot, *J. Colloid Interface Sci.* 2002, **255**, 293-298.
22 T. Fried, G. Shemer, G. Markovich, *Adv. Mater.* 2001, **13**, 1158-1161.
23 Z. J. Zhang, Z. L. Wang, B. C. Chakoumakos, J. S. Yin, *J. Am. Chem. Soc.* 1998, **120**, 1800-1804.
24 Z. X. Tang, C. M. Sorensen, K. J. Klabunde, G. C. Hadjipanayis, *J. Colloid Interface Sci.* 1991, **146**, 38-52.
25 C. Y. Hong, I. J. Jang. H. E. Horng, C. J. Hsu, Y. D. Yao, H. C. Yang, *J. Appl. Phys.* 1997, **81**, 4275-4277.
26 N. Moumen, M. P. Pileni, *J. Phys. Chem.* 1996, **100**, 1867-1873.
27 C. Liu, B. S. Zou, A. J. Rondinone, Z. J. Zhang, *J. Phys. Chem. B* 2000, **104**, 1141-1145.
28 Q. Liu, H. Huang, L. Lai, J. Sun, T. Shang, Q. Zhou, Z. Xu, *J. Mater. Sci.* 2009, **44**, 1187-1191.
29 S. H. Sun, H. Zeng, D. B. Robinson, S. Raoux, P. M. Rice, S. X. Wang, G. X. Li, *J. Am. Chem. Soc.* 2004, **126**, 273-279.
30 E. Kang, J. Park, Y. Hwang, M. Kang, J. G. Park, T. Hyeon, *J. Phys. Chem. B* 2004, **108**, 13932-13935.
31 H. Zeng, P. M. Rice, S. X. Wang, S. H. Sun, *J. Am. Chem. Soc.* 2004, **126**, 11458-11459.
32 M. Moriya, M. Ito, W. Sakamoto, T. Yogo, *Cryst. Growth Des.* 2009, **9**, 1889-1893.
33 J. Park, K. J. An, Y. S. Hwang, J. G. Park, H. J. Noh, J. Y. Kim, J. H. Park, N. M. Hwang, T. Hyeon, *Nat. Mater.* 2004, **3**, 891-895.
34 X. D. Yang, J. Li, J. Liu, Y. Tian, B. Li, K. Cao, S. Liu, M. Hou, S. Li, L. Ma, J. *J. Mater. Chem. A* 2014, **2**, 1550-1559.
35 S. S. Basarir, N. P. Bayramgil, *Cellulose* 2013, **20**, 827-839.
36 J. Qu, W. Li, C. Y. Cao, X. J. Yin, L. Zhao, J. Bai, Z. Qin, W. G. Song, *J. Mater. Chem.* 2012, **22**, 17222-17226.
37 K. Singh, C. Shah, C. Dwivedi, M. Kumar, P. N. Bajaj, *J. Appl. Polym. Sci.* 2013, **127**, 410-419.

38 J. Park, E. Kang, C. J. Bae, J.-G. Park, H.-J. Noh, J.-Y. Kim, J.-H. Park, H. M. Park, T. Hyeon, *J. Phys. Chem. B* 2004, **108**, 13594-13598.
39 A. Prakash, H. G. Zhu, C. J. Jones, D. N. Benoit, A. Z. Ellsworth, E. L. Bryant, V. L. Colvin, *ACS Nano* 2009, **3**, 2139-2146.
40 D. N. Benoit, H. G. Zhu, M. H. Lilierose, R. A. Verm, N. Ali, A. N. Morrison, J. D. Fortner, C. Ayendano, V. L. Colvin, *Anal. Chem.* 2012, **84**, 9238-9245.
41 R. A. Sperling, W. J. Parak, *Philos. Trans. R. Soc., A* 2010, **368**, 1333-1383.
42 E. Vigneau, C. Loisel, M. F. Devaux, P. Cantoni, *Powder Technol.* 2000, **107**, 243-250.
43 K. L. Chen, M. Elimelech, *Langmuir* **2006,** *22*, 10994-11001.
44 E. Illes, E. Tombacz, *J. Colloid Interface Sci.* 2006, **295**, 115-123.
45 J. D. Hu, Y. Zevi, X. M. Kou, J. Xiao, X. J. Wang, Y. Jin, *Sci. Total Environ.* 2010, **408**, 3477-3489.
46 K. L. Chen, B. A. Smith, W. P. Ball, D. H. Fairbrother, *Environ. Chem.* 2010, **7**, 10-27.
47 D. Jassby, M. Wiesner, *Langmuir* 2011, **27**, 902-908.
48 R. H. Kodama, A. E. Berkowitz, E. J. McNiff, S. Foner, *Phys. Rev. Lett.* 1996, **77**, 394-397.
49 C. Liu, B. S. Zou, A. J. Rondinone, J. Zhang, *J. Am. Chem. Soc.* 2000, **122**, 6263-6267.
50 M. N. Ashiq, M. J. Iqbal, I. H. Gul, *J. Magn. Magn. Mater.* 2011, **323**, 259-263.
51 T. Hyeon, Y. Chung, J. Park, S. S. Lee, Y. W. Kim, B. H. Park, *J. Phys. Chem. B* 2002, **106**, 6831-6833.
52 C. N. Chinnasamy, A. Narayanasamy, N. Ponpandian, K. Chattopadhyay, K. Shinoda, B. Jeyadevan, K. Tohji, K. Nakatsuka, T. Furubayashi, I. Nakatani, *Phys. Rev. B* 2001, 63.
53 W. Schiessl, W. Potzel, H. Karzel, M. Steiner, G. M. Kalvius, A. Martin, M. K. Krause, I. I. Halevy, J. Gal, W. Schafer, G. Will, M. Hillberg, R. Wappling, *Phys. Rev. B* 1996, **53**, 9143-9152.
54 E. S. Ilton, J. F. Boily, E. C. Buck, F. N. Skomurski, K. M. Rosso, C. L. Cahill, J. R. Bargar, A. R. Felmy, *Environ. Sci. Technol.* 2010, **44**, 170-176.
55 M. I. Boyanov, E. J. O'Loughlin, E. E. Roden, J. B. Fein, K. M. Kemner, *Geochim. Cosmochim. Acta* 2007, **71**, 1898-1912.
56 S. Bachmaf, B. Planer-Friedrich, B. J. Merkel, *Geochim. Cosmochim. Acta* 2009, **73**, A67-A67.
57 S. K. Kazy, S. F. D'Souza, P. Sar, *J. Hazard. Mater.* 2009, **163**, 65-72.
58 L. Wang,; Z. M. Yang, J. H. Gao, K. M. Xu, H. W. Gu, B. Zhang, X. X. Zhang, B. Xu, *J. Am. Chem. Soc.* 2006, **128**, 13358-13359.
59 M. Sutton, S. R Burastero, *Chem. Res. Toxicol.* 2004, **17**, 1468-1480.
60 S. J. Datta, W. K. Moon, D. Y.Choi, I. C. Hwang, K. B. Yoon, *Angew. Chem. Int. Ed.* 2014, **53**, 7203-7208.